



ARL-TR-8490 • SEP 2018



Coupling Molecular Dynamics and Machine Learning for Predicting Aluminum Segregation to Magnesium Grain Boundaries

by Mark A Tschopp, Kaushik Joshi, and Santanu Chaudhuri

Approved for public release; distribution is unlimited.

NOTICES

Disclaimers

The findings in this report are not to be construed as an official Department of the Army position unless so designated by other authorized documents.

Citation of manufacturer's or trade names does not constitute an official endorsement or approval of the use thereof.

Destroy this report when it is no longer needed. Do not return it to the originator.



Coupling Molecular Dynamics and Machine Learning for Predicting Aluminum Segregation to Magnesium Grain Boundaries

by Mark A Tschopp
Office of the Director, ARL

Kaushik Joshi and Santanu Chowdhury
University of Illinois–Chicago, Chicago, IL

REPORT DOCUMENTATION PAGE

Form Approved
OMB No. 0704-0188

Public reporting burden for this collection of information is estimated to average 1 hour per response, including the time for reviewing instructions, searching existing data sources, gathering and maintaining the data needed, and completing and reviewing the collection information. Send comments regarding this burden estimate or any other aspect of this collection of information, including suggestions for reducing the burden, to Department of Defense, Washington Headquarters Services, Directorate for Information Operations and Reports (0704-0188), 1215 Jefferson Davis Highway, Suite 1204, Arlington, VA 22202-4302. Respondents should be aware that notwithstanding any other provision of law, no person shall be subject to any penalty for failing to comply with a collection of information if it does not display a currently valid OMB control number.

PLEASE DO NOT RETURN YOUR FORM TO THE ABOVE ADDRESS.

1. REPORT DATE (DD-MM-YYYY) September 2018		2. REPORT TYPE Technical Report		3. DATES COVERED (From - To) October 2016–July 2018	
4. TITLE AND SUBTITLE Coupling Molecular Dynamics and Machine Learning for Predicting Aluminum Segregation to Magnesium Grain Boundaries				5a. CONTRACT NUMBER	
				5b. GRANT NUMBER	
				5c. PROGRAM ELEMENT NUMBER	
6. AUTHOR(S) Mark A Tschopp, Kaushik Joshi, and Santanu Chaudhuri				5d. PROJECT NUMBER	
				5e. TASK NUMBER	
				5f. WORK UNIT NUMBER	
7. PERFORMING ORGANIZATION NAME(S) AND ADDRESS(ES) US Army Research Laboratory ATTN: RDRL-D 1452 E 53rd Street, Chicago, IL 60615–4513				8. PERFORMING ORGANIZATION REPORT NUMBER ARL-TR-8490	
9. SPONSORING/MONITORING AGENCY NAME(S) AND ADDRESS(ES)				10. SPONSOR/MONITOR'S ACRONYM(S)	
				11. SPONSOR/MONITOR'S REPORT NUMBER(S)	
12. DISTRIBUTION/AVAILABILITY STATEMENT Approved for public release; distribution is unlimited.					
13. SUPPLEMENTARY NOTES					
14. ABSTRACT Engineering magnesium alloys for Army applications requires an understanding of corrosion behavior, including how grain boundaries (GBs) or second phases/intermetallics affect corrosion at the atomic scale. In magnesium–aluminum alloys, precipitation of the Mg ₁₇ Al ₁₂ phase at GBs can have important implications for mechanical and corrosion behavior, but first, single atom segregation to GBs is required. The objective of this study is to quantify the energetics of segregation of aluminum to a dataset of different symmetric tilt grain boundaries (STGBs) for magnesium. In this work, aluminum atoms were iteratively placed at various atomic sites within 20 Å of the GB center for a dataset of 30 {0001} STGBs. Results show how GB structure affects the energetics and length scales of aluminum segregation as well as the dependence of segregation energetics on the local atomic environment, which was used to form a surrogate (machine learning) model for segregation energetics. The ability to compute grain boundary physical properties of interest using machine learning techniques can have broad implications for the area of grain boundary science and engineering.					
15. SUBJECT TERMS molecular dynamics, grain boundary, magnesium, segregation					
16. SECURITY CLASSIFICATION OF:			17. LIMITATION OF ABSTRACT UU	18. NUMBER OF PAGES 40	19a. NAME OF RESPONSIBLE PERSON Mark A Tschopp
a. REPORT Unclassified	b. ABSTRACT Unclassified	c. THIS PAGE Unclassified			19b. TELEPHONE NUMBER (Include area code) 301-938-5389

Contents

List of Figures	iv
List of Tables	vii
1. Introduction	1
2. Simulation Methodology	3
2.1 Grain Boundary Dataset	3
2.2 Computational Cell and Boundary Conditions	3
2.3 Embedded Atom Method Potential	6
2.4 Grain Boundary Segregation	7
3. Simulation Results	9
3.1 Correlation with Local Environment Properties	16
3.2 Segregation Model Based on Local Environment Properties	20
4. Conclusion	26
5. References	27
List of Symbols, Abbreviations, and Acronyms	30
Distribution List	31

List of Figures

- Fig. 1 (left) The 3-D periodic bicrystal computational cell is shown for the $\{3\bar{2}10\}/\{\bar{1}\bar{2}30\}$ GB. For the purposes of showing the simulation cell, the GB was expanded by 20 and 50 period images in the GB period (X) and tilt (Y) directions, respectively. (right) Close-up of the atomic GB structure as viewed down the $\langle 0001 \rangle$ tilt direction, where the black lines indicate the simulation cell bounds for the GB period direction (i.e., normal to the tilt direction along the GB plane). In both images, the centrosymmetry parameter is used to color the atoms over the range of 9–11.....5
- Fig. 2 Schematic showing the effect of misorientation angle for the 30 $\langle 0001 \rangle$ GBs investigated in this study. The vertical lines delineate the transition from low-angle GBs ($\theta \leq 15^\circ$ and $\theta \geq 45^\circ$) to high-angle GBs ($15^\circ < \theta < 45^\circ$).5
- Fig. 3 Plot of the cohesive energy versus interatomic spacing for different crystal structures of magnesium using the Liu et al. EAM potential. From NIST interatomic potential website.²³6
- Fig. 4 Plot showing the change in the segregation energy as a function of the distance from the GB center in the $\{26, \bar{1}7, \bar{9}, 0\}/\{\bar{9}, \bar{1}7, 26, 0\}$ GB. The horizontal line represents the bulk segregation energy for aluminum in single crystal magnesium; positive energies are energetically favorable for aluminum in that site, negative energies are unfavorable for aluminum in that site. 10
- Fig. 5 Histogram of the segregation energies for substitutional aluminum for all GB sites from the 30 $\langle 0001 \rangle$ GBs within this study. The number of sites axis is limited to 1000 to show the peak in segregation energies above 0.20 eV. A large number of sites have segregation energies similar to bulk single crystal value (0.06 eV) since the cutoff for sites is up to 20 Å from the GB. 11
- Fig. 6 Image of the segregation energy as a function of spatial location within the GB region for the $\{26, \bar{1}7, \bar{9}, 0\}/\{\bar{9}, \bar{1}7, 26, 0\}$ GB as viewed along the $\langle 0001 \rangle$ tilt direction 12
- Fig. 7 Plots showing the change in the segregation energy as a function of the distance from the GB center for increasing GB misorientation angle within the $\langle 0001 \rangle$ STGB system: (a) $\{7\bar{4}\bar{3}0\}/\{\bar{3}470\}$ GB, (b) $\{3\bar{2}10\}/\{\bar{1}\bar{2}30\}$ GB, (c) $\{11, \bar{8}, \bar{3}, 0\}/\{\bar{3}, \bar{8}, 11, 0\}$ GB, (d) $\{9\bar{7}\bar{2}0\}/\{\bar{2}790\}$ GB, (e) $\{11, \bar{9}, \bar{2}, 0\}/\{\bar{2}, \bar{9}, 11, 0\}$ GB, and (f) $\{10, \bar{9}, \bar{1}, 0\}/\{\bar{1}, \bar{9}, 10, 0\}$ GB. The horizontal line represents the bulk segregation energy for aluminum in single crystal magnesium. 14

Fig. 8	Image of the segregation energy E_{seg} as a function of spatial location within the GB region for GBs with increasing GB misorientation angle within the $\langle 0001 \rangle$ STGB system: (top, left to right) $\{7\bar{4}30\}/\{3\bar{4}70\}$ GB, $\{3\bar{2}10\}/\{1\bar{2}30\}$ GB, $\{11, \bar{8}, \bar{3}, 0\}/\{\bar{3}, \bar{8}, 11, 0\}$ GB, and (bottom, left to right) $\{9\bar{7}20\}/\{2\bar{7}90\}$ GB, $\{11, \bar{9}, \bar{2}, 0\}/\{2, \bar{9}, 11, 0\}$ GB, $\{10, \bar{9}, \bar{1}, 0\}/\{\bar{1}, \bar{9}, 10, 0\}$ GB	15
Fig. 9	Correlation map between segregation energy and other common per atom variables: stress components, force components, Voronoi volume, centrosymmetry parameter, coordination number, atom coordinates, potential energy. (a) Correlation map of R , where $R = 1$ is perfect positive linear correlation and $R = -1$ is perfect negative linear correlation. (b) Correlation map of absolute value of R . In both maps, the variables are ordered using a hierarchical clustering technique using Euclidean distance between rows/columns.	17
Fig. 10	Plots of segregation energy as a function of (a) Voronoi volume, (b) hydrostatic stress, and (c) potential energy for all atomic sites in the $\langle 0001 \rangle$ STGB system. Notice the positive linear correlation for Voronoi volume and hydrostatic stress (which correlate with each other) and the negative linear correlation with the potential energy.	19
Fig. 11	Plots of model predictions against the atomistically calculated segregation energy for two different regression models based on the atomic metrics: (a) linear regression model and (b) quadratic regression model (with linear and interaction terms)	20
Fig. 12	(a) Plot of neural network model predictions against the atomistically calculated segregation energy, and (b) error histogram of the neural network model for the training set (70% of data), validation set (15%), and test set (15%)	21
Fig. 13	Image of the neural network prediction of segregation energy E_{seg}^{NN} as a function of spatial location within the GB region for GBs with increasing GB misorientation angle within the $\langle 0001 \rangle$ STGB system: (top, left to right) $\{7\bar{4}30\}/\{3\bar{4}70\}$ GB, $\{3\bar{2}10\}/\{1\bar{2}30\}$ GB, $\{11, \bar{8}, \bar{3}, 0\}/\{\bar{3}, \bar{8}, 11, 0\}$ GB, and (bottom, left to right) $\{9\bar{7}20\}/\{2\bar{7}90\}$ GB, $\{11, \bar{9}, \bar{2}, 0\}/\{2, \bar{9}, 11, 0\}$ GB, $\{10, \bar{9}, \bar{1}, 0\}/\{\bar{1}, \bar{9}, 10, 0\}$ GB. Compare with actual energies in Fig. 8.	22

Fig. 14 Image of the neural network prediction error of segregation energy ΔE_{seg} as a function of spatial location within the GB region for GBs with increasing GB misorientation angle within the $\langle 0001 \rangle$ STGB system: (top, left to right) $\{7\bar{4}30\}/\{\bar{3}470\}$ GB, $\{3\bar{2}10\}/\{\bar{1}230\}$ GB, $\{11, \bar{8}, \bar{3}, 0\}/\{\bar{3}, \bar{8}, 11, 0\}$ GB, and (bottom, left to right) $\{9\bar{7}20\}/\{\bar{2}790\}$ GB, $\{11, \bar{9}, \bar{2}, 0\}/\{\bar{2}, \bar{9}, 11, 0\}$ GB, $\{10, \bar{9}, \bar{1}, 0\}/\{\bar{1}, \bar{9}, 10, 0\}$ GB. To further accentuate the location and magnitude of error, the size of the atoms is scaled by increasing absolute value of error (scaled from minimal size to three times the size of those in Figs. 8 and 13 for every 0.10-eV error). 23

Fig. 15 Images of the neural network prediction of the segregation energy E_{seg}^{NN} as a function of spatial location for the 19,624 atoms in the $\{26, \bar{17}, \bar{9}, 0\}/\{\bar{9}, \bar{17}, 26, 0\}$ GB as viewed along the $\langle 0001 \rangle$ tilt direction. The bottom image is of the whole boundary, while the top image is a magnified view of part of the boundary. 25

List of Tables

Table 1	The misorientation angles and GB normals for the 30 $\langle 0001 \rangle$ GBs investigated in this study. The calculated magnesium GB energies are also given.	4
---------	--	---

1. Introduction

Engineering magnesium alloys for structural applications often requires an understanding of corrosion behavior,¹ including how grain boundaries (GBs) or second phases/intermetallics affect corrosion at the atomic scale. While there are a number of alloying elements that are added to magnesium to improve properties, aluminum is one of the elements that is often added in the highest concentrations for alloying with magnesium because of its significant effect on the hardness, strength, and castability of magnesium alloys. Aluminum is also known to impact corrosion resistance within magnesium alloys; in general, higher aluminum contents result in greater corrosion resistance. In magnesium–aluminum alloys, the precipitation of the $\text{Mg}_{17}\text{Al}_{12}$ phase at GBs can have important implications for mechanical and corrosion behavior. The motion of aluminum atoms within the magnesium matrix that leads to nucleation and growth of these phases is important to model the microstructure and its evolution for magnesium–aluminum alloys.

The microstructure of (polycrystalline) magnesium alloys plays a role in the evolution of these precipitates. GBs are a ubiquitous feature within all polycrystalline materials, affecting both the microstructure evolution and the properties of polycrystals. Not only is the inherent structure of the GB important for properties, but the presence of other elements at the GB can also significantly affect material properties. A number of prior studies have examined segregation of different elements to magnesium GBs and twin boundaries to understand the mechanisms responsible for the observed microstructures and properties in magnesium alloys. For instance, rare earth elements are known to have a significant role on the formation of the underlying grain structure, leading to both experimental and computational studies aimed at uncovering their role on microstructure. For instance, prior studies have examined segregation of yttrium to magnesium GBs and found that the presence of yttrium at the GBs reduced the heterogeneity in GB energy and mobility.² This reduction in mobility may be one of the main reasons for the randomized texture, as proposed by Barrett et al.³ and references therein. Of course, these studies are just one of many that show how rare earth elements have impacted creep resistance, corrosion resistance, and grain refinement. Understanding other elements such as aluminum within magnesium alloys is also critical to modeling the evolution of microstructure in magnesium and its effect on properties.

Modeling and simulation techniques can help with our fundamental understanding of how the local atomic environment of GBs influences the segregation of alloying elements—necessary to model the interaction between GB structure and alloying elements. Molecular dynamics (MD) simulations are often used to model GBs and these atomic interactions due to their ability to simulate large numbers of atoms within a computationally inexpensive framework. Interatomic potentials approximate the quantum mechanical interactions (i.e., the electronic contribution) between atoms, enabling the ability to efficiently interrogate the physics and kinetics at the atomic scale. Prior studies by Tschopp et al. have used molecular statics and MD simulations with copper and aluminum interatomic potentials to explore how various properties change as a function of GB structure and GB degrees of freedom, examining the structure, energy, and faceting,^{4–6} dislocation nucleation,^{7–9} and cohesive energy (fracture)^{10,11} of GBs. Additionally, prior molecular statics simulations have been used to compute the formation energies of point defects (vacancies and self-interstitial atoms^{12,13}) and the segregation energies of various elements (impurities,¹⁴ carbon,¹⁵ hydrogen,¹⁶ helium^{17–19}) as a function of GB site location.^{12–19} These methods can be expanded to quantifying properties as a function of local structure in magnesium GBs. Due to the ability to rapidly develop simulation databases for static quantities such as segregation energies, simulation results can then be combined with machine learning and data science techniques to mathematically represent atomic processes such as the energetics of segregation as a function of the local structure.

Given the importance of aluminum within magnesium alloys and the prevalence of GBs as a microstructure feature (that greatly affects properties), understanding how aluminum segregates to magnesium can shed light on the evolution of microstructure in magnesium. The objective of this study is to quantify the energetics of segregation of aluminum to a dataset of different symmetric tilt grain boundaries (STGBs) for magnesium. In this work, aluminum atoms were iteratively placed at various atomic sites within 20 Å of the GB center for a dataset of 30 $\langle 0001 \rangle$ STGBs (14231 sites). Results show how GB structure affects the energetics and length scales of aluminum segregation as well as the dependence of segregation energetics on the local atomic environment, which was used to form a surrogate model for segregation energetics.

2. Simulation Methodology

The simulation methodology consists of GB dataset generation, segregation simulations, and energetics calculations. These are described in the following subsections.

2.1 Grain Boundary Dataset

Table 1 lists all 30 $\langle 0001 \rangle$ STGBs studied in this research. The GBs were previously developed to examine texture formation during dynamic recrystallization in magnesium alloys.³ The GB misorientation angle θ between the two lattices also requires a reference direction for the 0° (single crystal) GB, which is the $[1210]$ direction in this case. Note that because of symmetry of the lattice, this means that the 60° GB is also a single crystal “GB”. The GB plane helps to completely define the degrees of freedom associated with the GBs; these are also given in $hkil$ format, as is common for hexagonal close-packed (hcp) lattices. The GB energy is also given.

2.2 Computational Cell and Boundary Conditions

The methodology for generating the computational cell, boundary conditions, and atomic configuration is similar to prior literature for other metal systems with GBs (e.g., in copper/aluminum^{4-6,20,21} and Fe^{12,13}). For further information, the reader is referred to Tschopp and McDowell⁴ or Tschopp et al.²¹ A computational cell with three-dimensional (3-D) periodic boundary conditions consisting of two grains was used to obtain the equilibrium 0-K GB structure, GB excess energy, and segregation energies. The simulation cell is shown in Fig. 1. While there are 3-D periodic boundary conditions, notice that there are two free surfaces (top and bottom) with a single GB in the middle of the simulation cell. There are no fixed regions of atoms within the computational cell, so the atoms are able to translate as needed during the energy minimization process. Additionally, the free surfaces allow for volume expansion at the GB and to relieve the internal pressure within the cell. The size of the computational cells must be large enough to eliminate any interaction between the GB and the free surfaces; the simulation cell dimensions are given in Table 1. The minimum period in the X and Y directions (i.e., the GB period and tilt directions contained in the GB plane) was chosen to reduce the size of the boundary region and the number of atoms in the simulations. This does not affect the GB excess energy calculations or the GB structure, but the periodic distance does affect the segregation calculations (and is increased, as explained later). The simulation cell boundaries in the X and Y directions are fixed to maintain the correct equilibrium

Table 1 The misorientation angles and GB normals for the 30 $\langle 0001 \rangle$ GBs investigated in this study. The calculated magnesium GB energies are also given.

θ	GB normals (hkl) ₁ / (hkl) ₂	X_{per} (Å)	Y_{per} (Å)	No. of atoms	GB energy (mJ/m ²)
6.01°	(11, $\bar{6}$, $\bar{5}$, 0) ₁ / ($\bar{5}$, $\bar{6}$, 11, 0) ₂	52.8	5.2	8195	154.7
7.34°	(9, $\bar{5}$, $\bar{4}$, 0) ₁ / ($\bar{4}$, $\bar{5}$, 9, 0) ₂	43.2	5.2	6722	173.3
9.43°	(7, $\bar{4}$, $\bar{3}$, 0) ₁ / ($\bar{3}$, $\bar{4}$, 7, 0) ₂	33.7	5.2	5229	198.5
10.99°	(12, $\bar{7}$, $\bar{5}$, 0) ₁ / ($\bar{5}$, $\bar{7}$, 12, 0) ₂	57.8	5.2	8942	216.2
13.17°	(5, $\bar{3}$, $\bar{2}$, 0) ₁ / ($\bar{2}$, $\bar{3}$, 5, 0) ₂	24.1	5.2	3764	236.6
13.42°	(6, $\bar{4}$, $\bar{3}$, 0) ₁ / ($\bar{3}$, $\bar{4}$, 6, 0) ₂	30.5	5.2	4726	209.7
16.43°	(8, $\bar{5}$, $\bar{3}$, 0) ₁ / ($\bar{3}$, $\bar{5}$, 8, 0) ₂	38.7	5.2	6008	264.7
17.90°	(11, $\bar{7}$, $\bar{4}$, 0) ₁ / ($\bar{4}$, $\bar{7}$, 11, 0) ₂	53.4	5.2	8307	275.8
18.73°	(14, $\bar{9}$, $\bar{5}$, 0) ₁ / ($\bar{5}$, $\bar{9}$, 14, 0) ₂	68.0	5.2	10486	282.9
20.15°	(26, $\bar{17}$, $\bar{9}$, 0) ₁ / ($\bar{9}$, $\bar{17}$, 26, 0) ₂	126.6	5.2	19624	291.1
21.79°	(3, $\bar{2}$, $\bar{1}$, 0) ₁ / ($\bar{1}$, $\bar{2}$, 3, 0) ₂	14.6	5.2	2279	294.7
25.04°	(13, $\bar{9}$, $\bar{4}$, 0) ₁ / ($\bar{4}$, $\bar{9}$, 13, 0) ₂	63.8	5.2	9941	319.3
26.01°	(10, $\bar{7}$, $\bar{3}$, 0) ₁ / ($\bar{3}$, $\bar{7}$, 10, 0) ₂	49.2	5.2	7634	321.5
27.80°	(14, $\bar{10}$, $\bar{4}$, 0) ₁ / ($\bar{4}$, $\bar{10}$, 14, 0) ₂	69.1	5.2	10760	318.6
27.80°	(7, $\bar{5}$, $\bar{2}$, 0) ₁ / ($\bar{2}$, $\bar{5}$, 7, 0) ₂	34.6	5.2	5370	280.8
29.41°	(11, $\bar{8}$, $\bar{3}$, 0) ₁ / ($\bar{3}$, $\bar{8}$, 11, 0) ₂	54.5	5.2	8431	341.2
30.16°	(15, $\bar{11}$, $\bar{4}$, 0) ₁ / ($\bar{4}$, $\bar{11}$, 15, 0) ₂	74.5	5.2	11543	336.9
32.20°	(4, $\bar{3}$, $\bar{1}$, 0) ₁ / ($\bar{1}$, $\bar{3}$, 4, 0) ₂	20.0	5.2	3101	288.0
34.54°	(13, $\bar{10}$, $\bar{3}$, 0) ₁ / ($\bar{3}$, $\bar{10}$, 13, 0) ₂	65.3	5.2	10112	283.9
35.57°	(9, $\bar{7}$, $\bar{2}$, 0) ₁ / ($\bar{2}$, $\bar{7}$, 9, 0) ₂	45.3	5.2	7024	283.3
38.21°	(5, $\bar{4}$, $\bar{1}$, 0) ₁ / ($\bar{1}$, $\bar{4}$, 5, 0) ₂	25.4	5.2	3943	253.9
40.35°	(11, $\bar{9}$, $\bar{2}$, 0) ₁ / ($\bar{2}$, $\bar{9}$, 11, 0) ₂	56.2	5.2	8758	255.8
42.10°	(6, $\bar{5}$, $\bar{1}$, 0) ₁ / ($\bar{1}$, $\bar{5}$, 6, 0) ₂	30.8	5.2	4795	253.7
43.57°	(13, $\bar{11}$, $\bar{2}$, 0) ₁ / ($\bar{2}$, $\bar{11}$, 13, 0) ₂	67.1	5.2	10446	229.9
44.82°	(7, $\bar{6}$, $\bar{1}$, 0) ₁ / ($\bar{1}$, $\bar{6}$, 7, 0) ₂	36.3	5.2	5614	224.7
46.83°	(8, $\bar{7}$, $\bar{1}$, 0) ₁ / ($\bar{1}$, $\bar{7}$, 8, 0) ₂	13.9	5.2	2161	207.6
49.58°	(10, $\bar{9}$, $\bar{1}$, 0) ₁ / ($\bar{1}$, $\bar{9}$, 10, 0) ₂	52.8	5.2	8189	186.0
51.39°	(12, $\bar{11}$, $\bar{1}$, 0) ₁ / ($\bar{1}$, $\bar{11}$, 12, 0) ₂	63.8	5.2	9889	169.4
52.07°	(13, $\bar{12}$, $\bar{1}$, 0) ₁ / ($\bar{1}$, $\bar{12}$, 13, 0) ₂	69.4	5.2	10742	161.6

magnesium lattice constant in the bulk crystal lattice regions.

In this study, Fig. 2 shows the change in GB energy as a function of GB misorientation angle. The two vertical lines serve as a cutoff between low-angle GBs and high-angle GBs. Because of symmetry of the hcp lattice, misorientation angles between 45° and 60° are also low-angle boundaries. The computed GB misorientation–energy curve is similar to work in the past, displaying only a few minor cusps in the energy relationship.

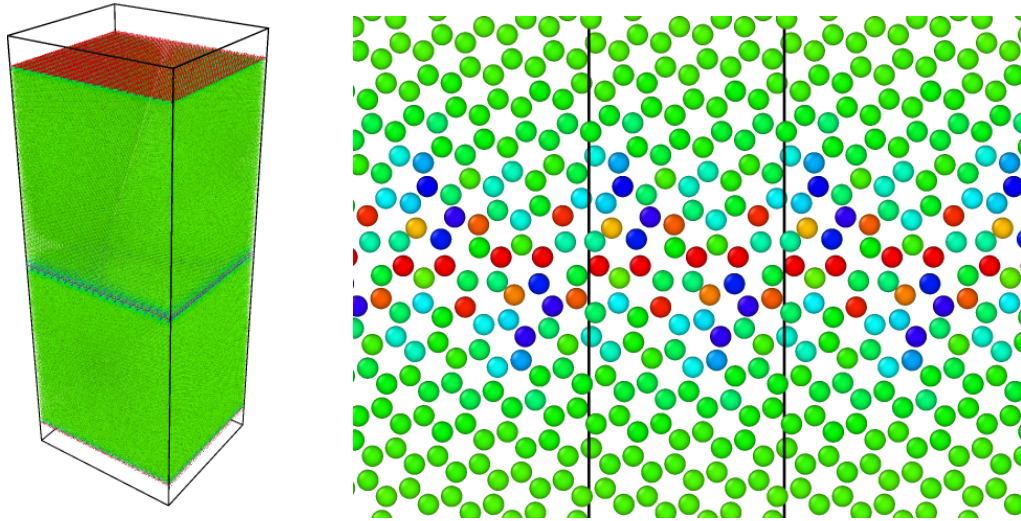


Fig. 1 (left) The 3-D periodic bicrystal computational cell is shown for the $\{3\bar{2}10\}/\{1\bar{2}30\}$ GB. For the purposes of showing the simulation cell, the GB was expanded by 20 and 50 period images in the GB period (X) and tilt (Y) directions, respectively. (right) Close-up of the atomic GB structure as viewed down the $\langle 0001 \rangle$ tilt direction, where the black lines indicate the simulation cell bounds for the GB period direction (i.e., normal to the tilt direction along the GB plane). In both images, the centrosymmetry parameter is used to color the atoms over the range of 9–11.

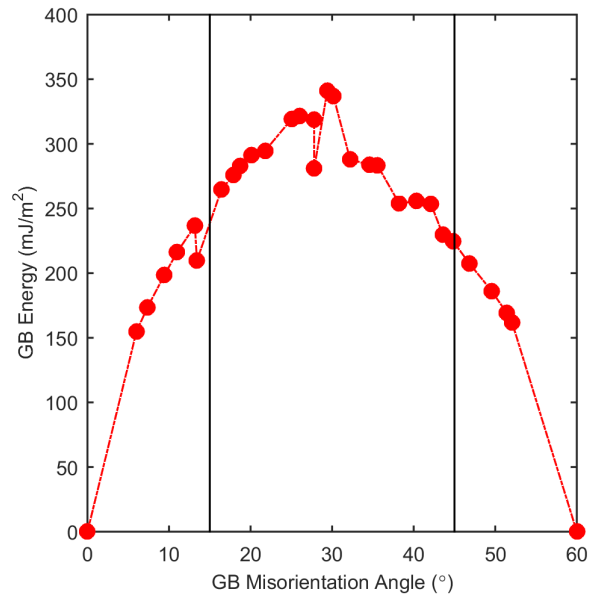


Fig. 2 Schematic showing the effect of misorientation angle for the 30 $\langle 0001 \rangle$ GBs investigated in this study. The vertical lines delineate the transition from low-angle GBs ($\theta \leq 15^\circ$ and $\theta \geq 45^\circ$) to high-angle GBs ($15^\circ < \theta < 45^\circ$).

2.3 Embedded Atom Method Potential

An embedded atom method (EAM) potential for magnesium²² was used for this study. This potential was fit using a force matching method with a large quantum mechanical database to give the correct physical properties for the magnesium–aluminum system, including the anisotropy of surface segregation characteristics, dilute heats, and heats of formation of intermetallics, to name a few. The computed anisotropy of surface segregation at low index surfaces agrees with experiments.²² In addition to segregation characteristics, the calculated stacking fault energies for the magnesium–aluminum potential are consistent with experimental data and ab initio calculations. The stacking fault energy landscape is important for GB structures, which are characterized by various full and partial dislocations. Figure 3 plots the cohesive energy versus interatomic spacing for a number of crystal structures in magnesium. The structures are generated based on the ideal atomic positions and b/a and c/a lattice parameter ratios for a given crystal prototype. The size of the system is then uniformly scaled, and the energy calculated without relaxing the system. To obtain these plots, 200 values of r are evaluated between 2.0 Å and 6.0 Å.

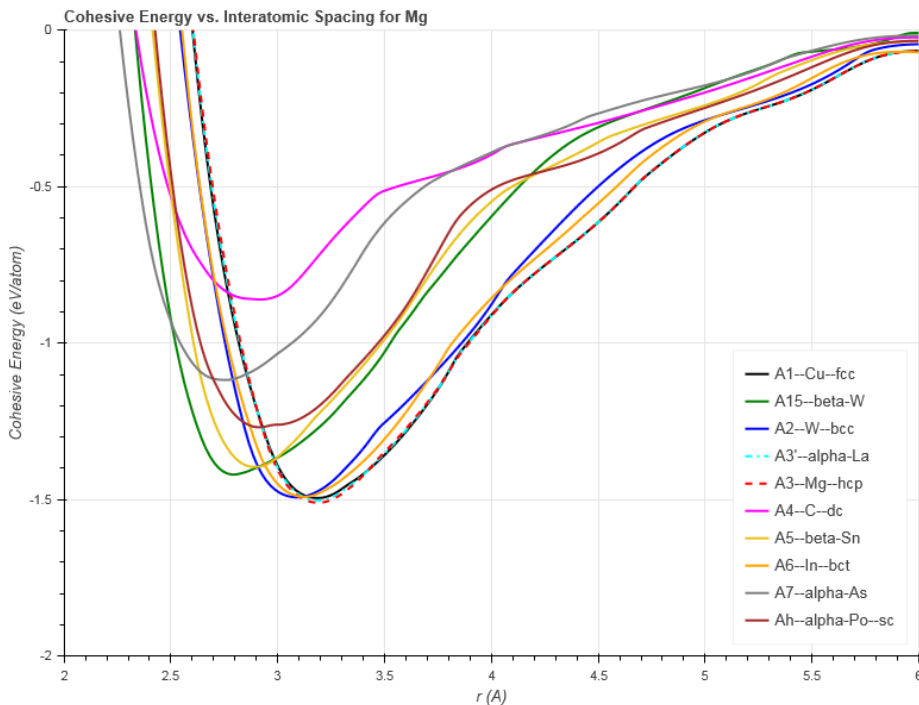


Fig. 3 Plot of the cohesive energy versus interatomic spacing for different crystal structures of magnesium using the Liu et al. EAM potential. From NIST interatomic potential website.²³

2.4 Grain Boundary Segregation

The formation energies of point defects and the segregation energies of various elements (impurities, carbon, hydrogen, helium) have been computed as a function of GB site location in prior work.¹²⁻¹⁹ In these sorts of simulations, there are two types of atom/defect replacements that can occur: on-lattice and off-lattice. The on-lattice replacement is similar to that pursued herein, while the off-lattice replacement needs to utilize various stochastic placement strategies to circumvent potential local minima.^{15,19}

In a similar manner, this study found that the segregation energy is affected for simulation cell periodic lengths below 10 Å. That is, the periodic image of the defect can actually significantly affect the defect's formation energy. Hence, multiple replications in the GB tilt direction and the GB period direction were used so that the periodic length in the GB plane directions were at least 10 Å. However, in subsequent figures, only the initial periodic structures are shown.

This work focuses on substitutional aluminum segregation to magnesium GBs and the effect of GB structure on aluminum segregation. In terms of methodology, for substitutional aluminum, the aluminum atom is simply added in the exact location of the removed magnesium atom. However, of particular interest in this study is both how the segregation energies change as a function of spatial location of sites and their proximity to the GB. The segregation energy for substitutional aluminum (Al) at site α in a magnesium (Mg) GB is given by

$$E_{seg}^{Al,\alpha} = \left(E_{tot}^{Al,\alpha} + E_c^{Mg} \right) - \left(E_{tot}^{GB} + E_c^{Al} \right). \quad (1)$$

Here, $E_{tot}^{Al,\alpha}$ is the total energy of the GB configuration with the substitutional aluminum at site α , E_{tot}^{GB} is the total energy of the GB without any Al, and E_c^{Mg} and E_c^{Al} are the cohesive energies of hcp magnesium and face-centered cubic (fcc) aluminum, respectively. The present potential yields cohesive energies of -1.5100 eV and -3.3601 eV for hcp magnesium and fcc aluminum, respectively, which is in agreement with previous studies²² as well as the National Institute of Standards and Technology (NIST) Interatomic Potential Repository.²³ In some cases, this is also called a formation energy, which typically uses a similar formulation that is often the reverse of Eq. 1, i.e.,

$$E_f^{Al,\alpha} = (E_{tot}^{GB} + E_c^{Al}) - (E_{tot}^{Al,\alpha} + E_c^{Mg}). \quad (2)$$

The binding energy of two substitutional aluminum atoms, both with the GB and with each other, is also of interest. The total binding energy of an aluminum atom interacting with another aluminum atom can be directly calculated from the formation (segregation) energies of the two atoms independent of one another. The binding energy is defined as the energy difference between the system where the aluminum atoms interact and the system where the aluminum atoms are far away from each other without any interaction. In the present case, though, the formation energy for a specific substitutional aluminum atom changes as a function of its location within the GB. Therefore, the binding energy between two substitutional aluminum atoms, for instance, may be different in the presence of a GB than in a perfect single crystal lattice. Two types of binding energies will be calculated in the present study: binding of aluminum atoms to the GB and binding of two aluminum atoms with each other (in the presence of a GB). As an example of aluminum atoms binding to the GB, the binding energy for a substitutional aluminum atom at site α to the GB is given by

$$E_b^{Al,\alpha} = E_f^{Al,bulk} - E_f^{Al,\alpha}, \quad (3)$$

where $E_f^{Al,bulk}$ and $E_f^{Al,\alpha}$ are the formation energies of a single substitutional aluminum atom either in the bulk or at site α , respectively. As an example of defects binding with each other, the binding energy for two first nearest neighbor (1nn) substitutional aluminum atoms at sites α and β is given by

$$E_b^{Al^\alpha,Al^\beta} = (E_f^{Al,\alpha} + E_f^{Al,\beta}) - E_f^{Al,\alpha,Al,\beta}. \quad (4)$$

Here, $E_f^{Al,\alpha}$ and $E_f^{Al,\beta}$ are the formation energies of a single substitutional aluminum atom at either site α or β , respectively, and $E_f^{Al,\alpha,Al,\beta}$ is the formation energy of two 1nn substitutional aluminum atoms at sites α and β . In these equations, it can be seen that a positive binding energy represents that it is energetically favorable for the two defects to interact, while a negative binding energy represents that the two defects prefer not to interact. To aid with interpreting results, we have used

both segregation energy and binding energy because for both of these quantities, a positive value means that it is more energetically favorable.

3. Simulation Results

Aluminum is examined in substitutional sites within 20 Å of the GB plane. The segregation energies for substitutional aluminum as a function of distance from the GB center are shown in Fig. 4 for the $\{26, \bar{1}7, \bar{9}, 0\}/\{\bar{9}, \bar{1}7, 26, 0\}$ GB in the $\langle 0001 \rangle$ STGB system. First, the GB center is found (using a criterion based on the excess cohesive energies of the atoms in the GB region) and the Z coordinates normal to the GB are scaled relative to that GB central plane. Hence, there are positive and negative values for distance to the GB center. Second, the line represents the bulk segregation energy to compare between different sites in the GB and the bulk behavior. There are a number of sites that are both favorable and unfavorable (binding energy) with respect to the bulk value, and these values appear symmetrically distributed about the GB plane (i.e., distance from GB of 0 in Fig. 4). In fact, there is almost an equal distribution of sites with energetically favorable and unfavorable segregation energies compared to bulk. In fact, Fig. 5 is a histogram of the segregation energies for all sites within this study (of 14231 sites). Over all GBs in this study, there is an equal number of sites that are above and below the bulk segregation energy values. This is perhaps not surprising given that GBs consist of dislocations, which have both tensile and compressive stress regions surrounding them that may attract/repel point defects, substitutional atoms, and impurities.

The spatial arrangement of segregation energies for substitutional aluminum is shown in Fig. 6 for the same $\{26, \bar{1}7, \bar{9}, 0\}/\{\bar{9}, \bar{1}7, 26, 0\}$ GB in the $\langle 0001 \rangle$ STGB system. In this image, each site represents the segregation energy of substitutional aluminum from a different simulation. The minimum periodic length is shown along the horizontal axis and the length from top to bottom is 40 Å, with the GB plane centered in the vertical direction. The scale bar for segregation energy is shown to the right of the image; the colors are chosen such that white is centered at the bulk value with red and blue representing above and below the bulk value, respectively. There are several findings to notice in this image. First, the atoms far away from the boundary are white, representing that the segregation energy of aluminum is ≈ 0.06 eV, the bulk segregation energy for the magnesium–aluminum potential. The deviation from bulk values is denoted by the color of the sites, with blue representing

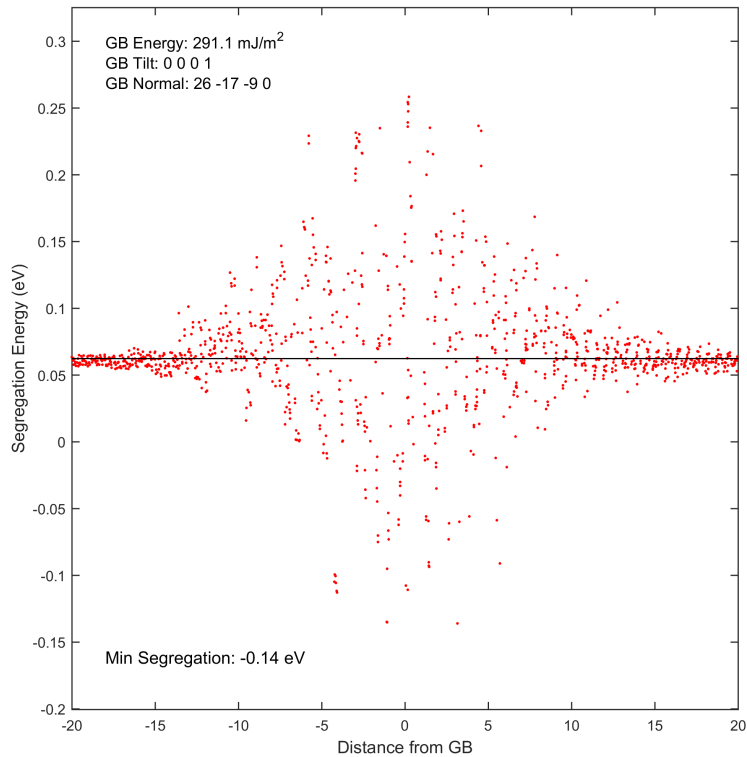


Fig. 4 Plot showing the change in the segregation energy as a function of the distance from the GB center in the $\{26, \bar{1}7, \bar{9}, 0\}/\{\bar{9}, \bar{1}7, 26, 0\}$ GB. The horizontal line represents the bulk segregation energy for aluminum in single crystal magnesium; positive energies are energetically favorable for aluminum in that site, negative energies are unfavorable for aluminum in that site.

a higher segregation energy and red representing a lower segregation energy. In general, most GBs have both sites with lower and higher segregation energies for substitutional aluminum (as shown in Fig. 5 also), which deviate from bulk values the most along the GB plane. Last, the maximum and minimum segregation energies are distributed throughout the GB plane.

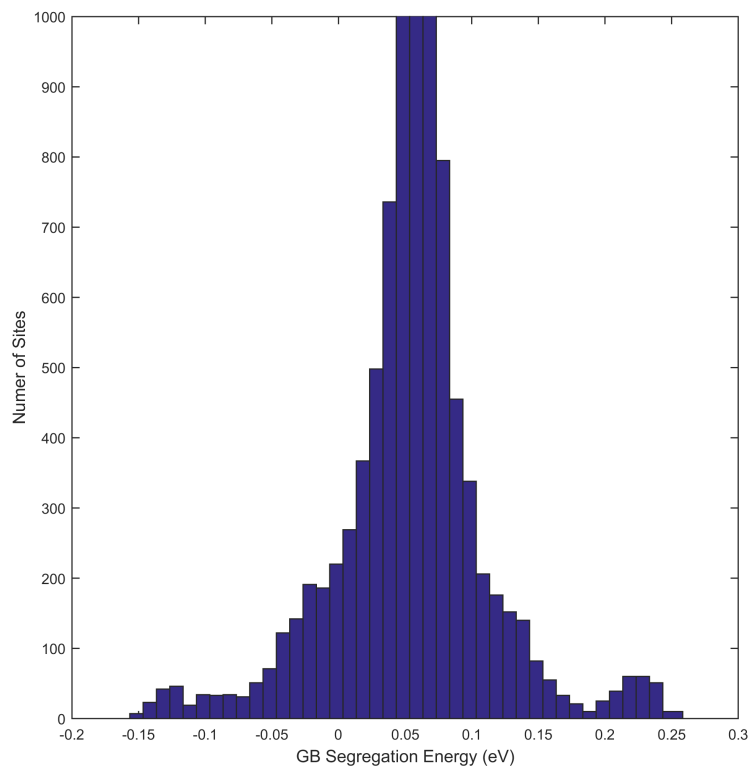


Fig. 5 Histogram of the segregation energies for substitutional aluminum for all GB sites from the 30 $\langle 0001 \rangle$ GBs within this study. The number of sites axis is limited to 1000 to show the peak in segregation energies above 0.20 eV. A large number of sites have segregation energies similar to bulk single crystal value (0.06 eV) since the cutoff for sites is up to 20 Å from the GB.

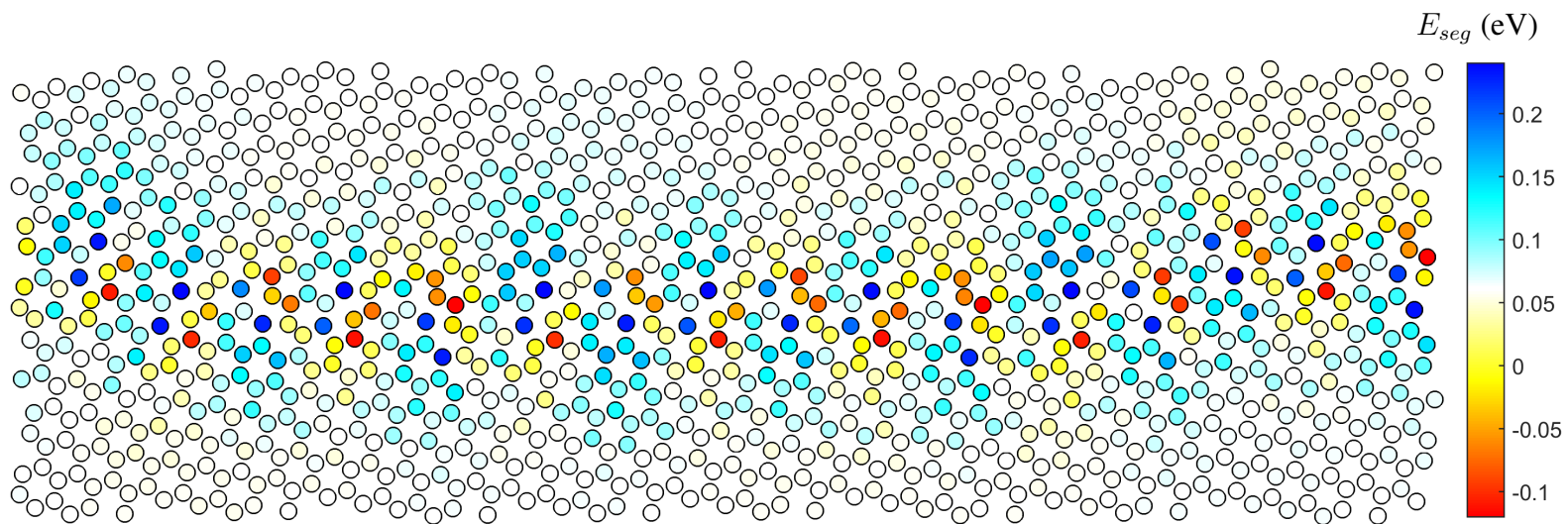


Fig. 6 Image of the segregation energy as a function of spatial location within the GB region for the $\{26, \bar{17}, \bar{9}, 0\}/\{\bar{9}, \bar{17}, 26, 0\}$ GB as viewed along the $\langle 0001 \rangle$ tilt direction

The segregation energies for substitutional aluminum as a function of distance from the GB center for increasing GB misorientation angle within the $\langle 0001 \rangle$ STGB system is shown in Fig. 7. As in Fig. 4, the Z coordinates normal to the GB are scaled relative to that GB central plane, and there are both positive and negative values for distance to the GB center. Again, the sites have segregation energies that are symmetrically distributed about the GB plane. Qualitatively, there is not a significant difference in the segregation energies as a function of misorientation angle in terms of the change in the magnitude of the segregation energies as a function of distance from the boundary. It should be noted that Figs. 7a and 7f are both low-angle GBs. There is a noticeable difference between low- and high-angle GBs, though. The low-angle boundaries are more dissociated into the bulk lattice than the high-angle GBs, which take on a more compact dislocation structure as the dislocation spacing is decreased.

The spatial arrangement of segregation energies for substitutional aluminum is shown in Fig. 8 for the same GBs with increasing misorientation angles within the $\langle 0001 \rangle$ STGB system. The segregation energies clearly show the individual dislocations comprising the low-angle GBs in Fig. 8, where the GB in the upper left of Fig. 8 is inclined with respect to the GB plane and the GB in the lower right of Fig. 8 is orthogonal to the GB plane. As in Fig. 7, the low-angle boundaries are more dissociated into the bulk lattice than the “more compact” high-angle GBs. The dislocation spacing associated with the low-angle boundaries is also clearly shown.

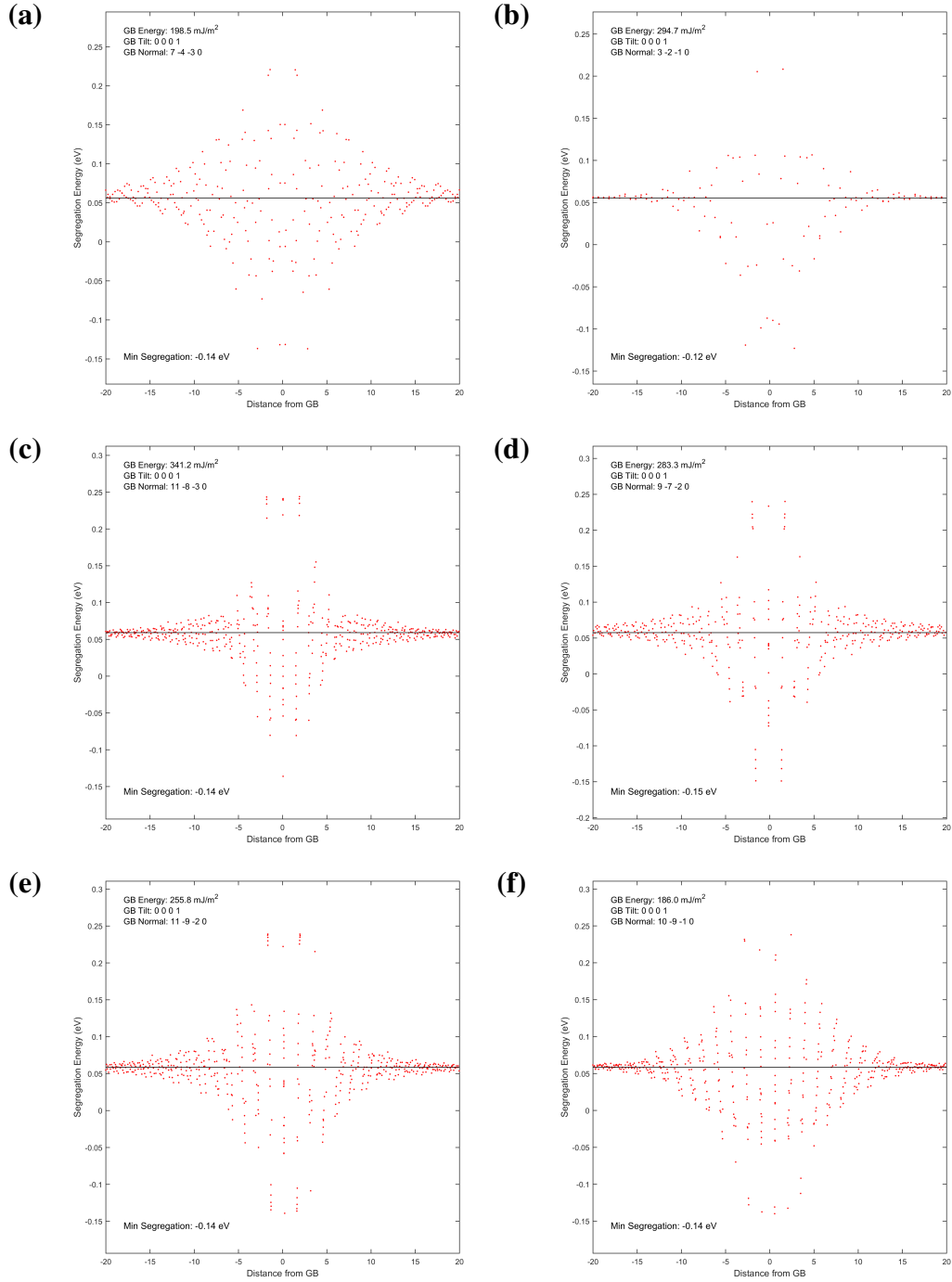


Fig. 7 Plots showing the change in the segregation energy as a function of the distance from the GB center for increasing GB misorientation angle within the $\langle 0001 \rangle$ STGB system: (a) $\{7\bar{4}30\}/\{3\bar{4}70\}$ GB, (b) $\{3\bar{2}\bar{1}0\}/\{\bar{1}\bar{2}30\}$ GB, (c) $\{11, \bar{8}, \bar{3}, 0\}/\{\bar{3}, \bar{8}, 11, 0\}$ GB, (d) $\{9\bar{7}20\}/\{\bar{2}\bar{7}90\}$ GB, (e) $\{11, \bar{9}, \bar{2}, 0\}/\{\bar{2}, \bar{9}, 11, 0\}$ GB, and (f) $\{10, \bar{9}, \bar{1}, 0\}/\{\bar{1}, \bar{9}, 10, 0\}$ GB. The horizontal line represents the bulk segregation energy for aluminum in single crystal magnesium.

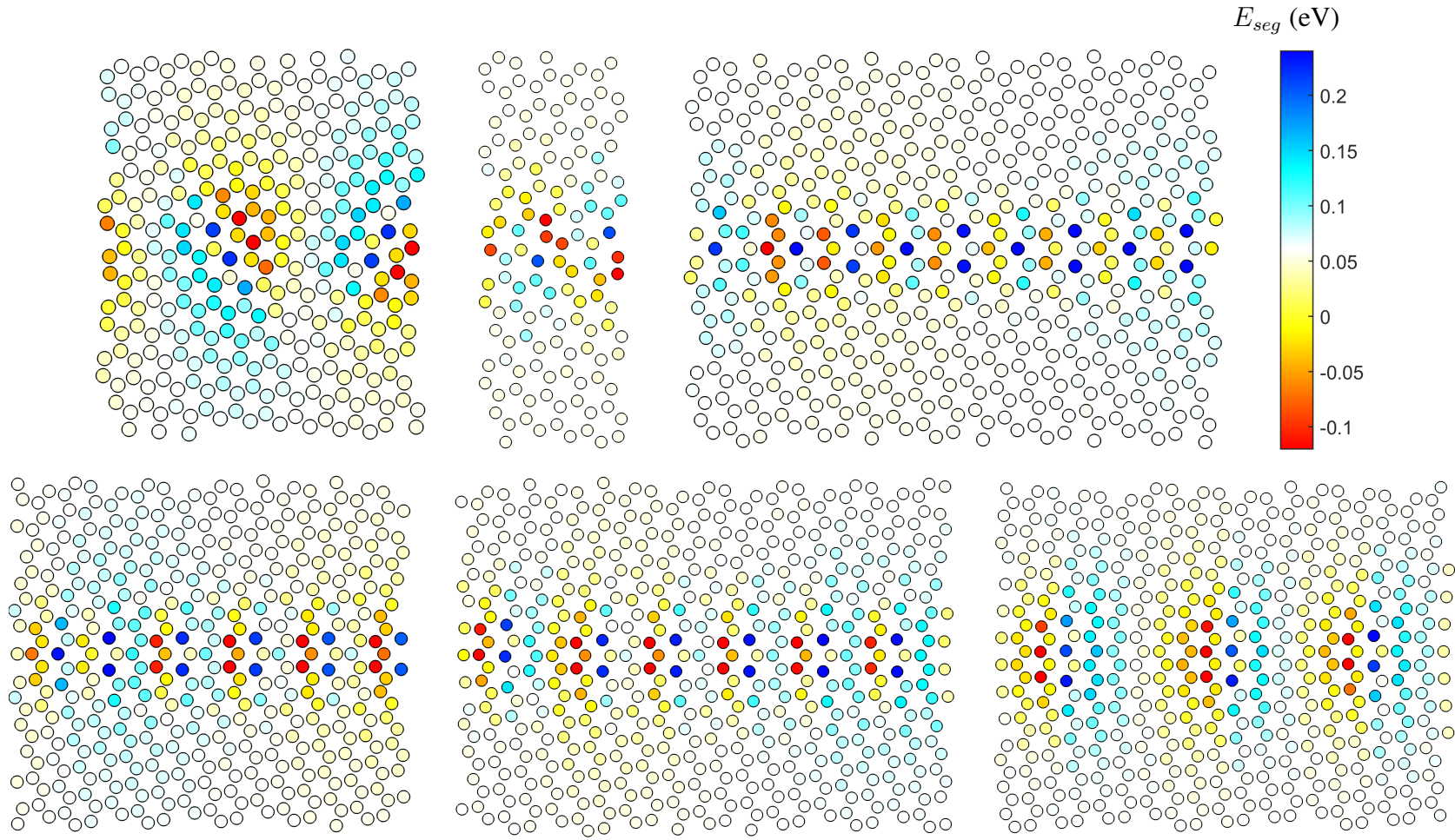


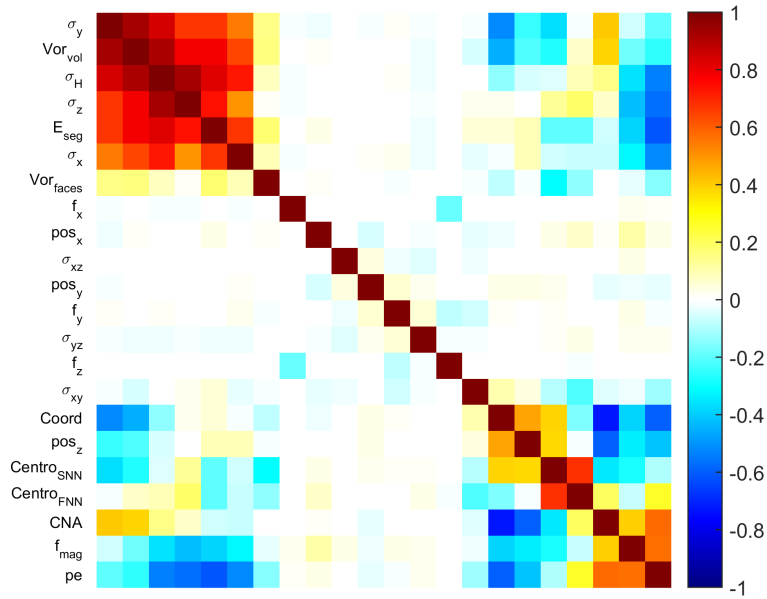
Fig. 8 Image of the segregation energy E_{seg} as a function of spatial location within the GB region for GBs with increasing GB misorientation angle within the $\langle 0001 \rangle$ STGB system: (top, left to right) $\{7\bar{4}30\}/\{3\bar{4}70\}$ GB, $\{3\bar{2}\bar{1}0\}/\{\bar{1}230\}$ GB, $\{11, \bar{8}, \bar{3}, 0\}/\{\bar{3}, \bar{8}, 11, 0\}$ GB, and (bottom, left to right) $\{9\bar{7}20\}/\{2\bar{7}90\}$ GB, $\{11, \bar{9}, \bar{2}, 0\}/\{2, \bar{9}, 11, 0\}$ GB, $\{10, \bar{9}, \bar{1}, 0\}/\{\bar{1}, \bar{9}, 10, 0\}$ GB

3.1 Correlation with Local Environment Properties

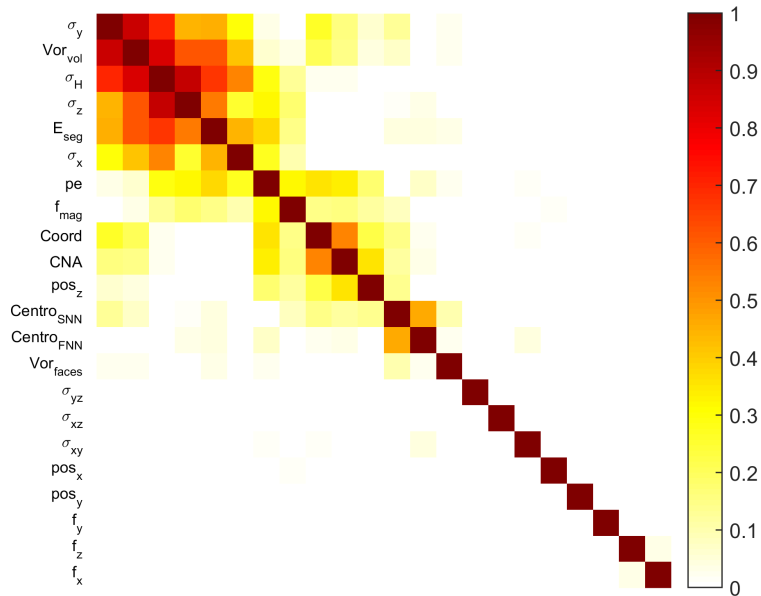
The local environment surrounding each atomic site at the GB influences the energetics associated with segregation of aluminum atoms. In this subsection, various per-atom local metrics that are readily available in the atomistic code LAMMPS are computed to compare with the segregation energies of aluminum at all sites in this study. Not only will any correlations between segregation energies and local environmental descriptors be of interest, but it is also informative to compute correlations between the different local environmental descriptors with themselves. The environmental descriptors used in this study can be categorized into geometric descriptors (Voronoi volume Vor_{vol} , Voronoi faces Vor_{faces} , position $pos_{x,y,z}$, coordination number $Coord$, first- and second-nearest neighbor centrosymmetry parameter $Centro_{FNN,SNN}$, common neighbor analysis CNA) and potential-based descriptors (potential energy pe , force $f_{x,y,z}$, and stress-based metrics $\sigma_{x,y,z,xy,xz,yz}$, including the hydrostatic stress σ_H).

The correlation matrices for the various local environmental descriptors (after hierarchically clustering the metrics) are shown in Fig. 9 for (a) the linear correlation coefficient R and (b) the absolute value of R . In Fig. 9a, the high positive linear correlations are between the directional stress components $\sigma_{x,y,z}$, the hydrostatic stress component, the Voronoi volume, and the segregation energy. The correlation between the stress components in x, y, and z directions and the hydrostatic stress is as expected, given that the hydrostatic stress is a function of these components, i.e., $\sigma_H = 1/3(\sigma_x + \sigma_y + \sigma_z)$. Another high correlation that could be expected is the centrosymmetry parameter calculated from the first nearest neighbors and the second nearest neighbors. Some of the highest negative correlations are between the potential energy of each magnesium atom and the coordination number, stress components (including hydrostatic stress), and the segregation energy. There is a lack of appreciable correlation for the force components, off-diagonal components of the stress tensor, and position, which may be due to minimal variation in these metrics or that there should not be a correlation (i.e., position is not translation or rotation invariant and a correlation is not expected). Figure 9b shows the correlation matrix for the absolute value of R after hierarchical clustering. Since the segregation energy is the computed property (that will later be predicted), this matrix shows that σ_H , Vor_{vol} , pe , and f_{mag} have some degree of linear correlation with segregation energy. This matrix also clearly shows that the force components, off-diagonal

components of the stress tensor, and position have negligible correlation with other local environmental descriptors.



(a)



(b)

Fig. 9 Correlation map between segregation energy and other common per atom variables: stress components, force components, Voronoi volume, centrosymmetry parameter, coordination number, atom coordinates, potential energy. (a) Correlation map of R , where $R = 1$ is perfect positive linear correlation and $R = -1$ is perfect negative linear correlation. (b) Correlation map of absolute value of R . In both maps, the variables are ordered using a hierarchical clustering technique using Euclidean distance between rows/columns.

The plots in Fig. 10 show an example of expanding a few of the correlation coefficients in the matrix (Fig. 9) to the entire dataset for three different local environmental descriptors: (a) Voronoi volume ($R^2 = 0.784$), (b) hydrostatic stress ($R^2 = 0.821$), and (c) potential energy ($R^2 = -0.617$). In these plots, each data point represents an atomic site within the dataset in which an aluminum atom was substituted for the magnesium atom. As described before, the x-axis metrics are those calculated prior to substituting the aluminum atom, minimizing the configuration, and calculating the segregation energy. The high density of points is around the Voronoi volume, hydrostatic stress, and potential energy in the bulk environment (22.94 \AA^3 , 0 GPa , and -1.51 eV , respectively). An increase in Voronoi volume or hydrostatic increases the aluminum segregation energy, and an increase in potential energy decreases the aluminum segregation energy.

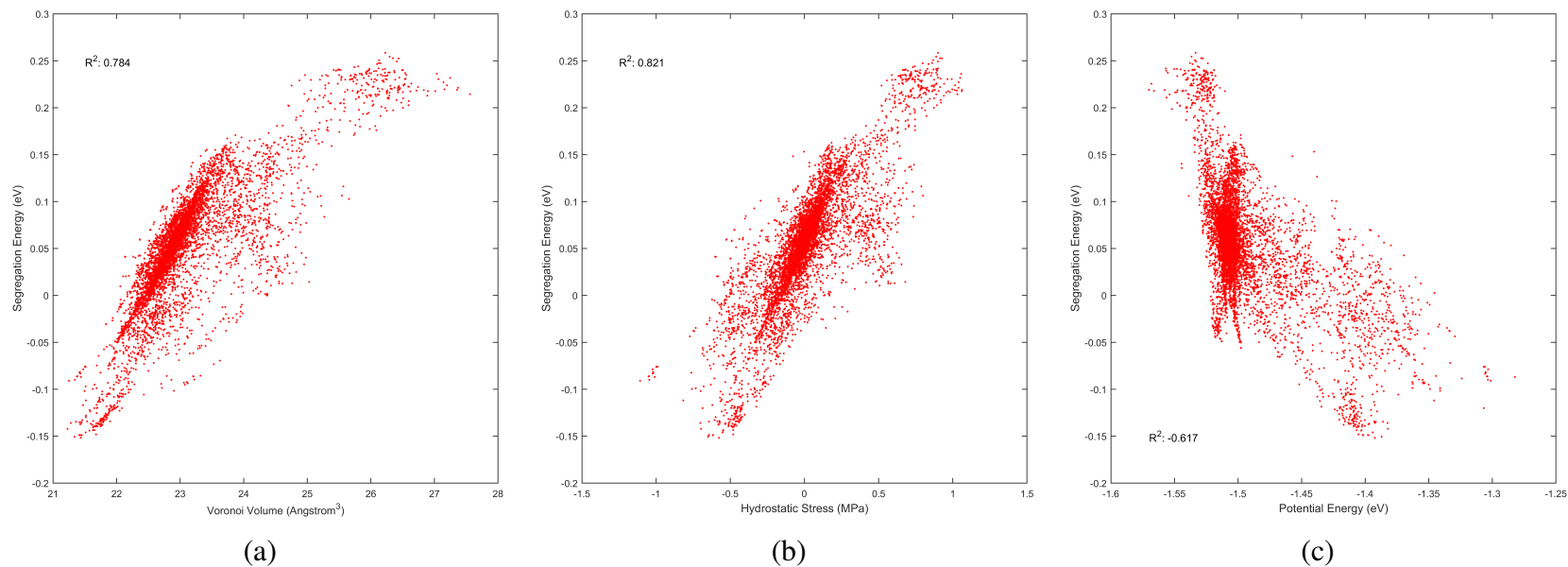


Fig. 10 Plots of segregation energy as a function of (a) Voronoi volume, (b) hydrostatic stress, and (c) potential energy for all atomic sites in the $\langle 0001 \rangle$ STGB system. Notice the positive linear correlation for Voronoi volume and hydrostatic stress (which correlate with each other) and the negative linear correlation with the potential energy.

3.2 Segregation Model Based on Local Environment Properties

Given that there is strong correlation ($R > 0.8$) between several local environment metrics and the segregation energy, a predictive model for this relationship can be fit. For instance, in this dataset, there are segregation energies (Y 's) and a vector of local environmental metrics (x_i 's) for each atom site (14,231). Supervised machine learning methods, also called surrogate models, are a class of models often used to describe the function f that mathematically describes this relationship (i.e., $Y = f(x_i)$). In this subsection, we use simple regression models and a neural network model to predict the segregation energy from local environmental metrics.

Figure 11 shows how the predicted segregation energies from two regression models capture the atomistically-calculated segregation energy. In general, the linear regression model in Fig. 11a predicts the segregation energies quite well ($R^2 = 0.878$); the quadratic regression model with linear ($\sum_i c_i x_i$), quadratic ($\sum_i c_i x_i^2$), and interaction coefficients ($\sum_i \sum_j c_i x_i x_j$) predicts the segregation energies even better ($R^2 = 0.935$), as expected.

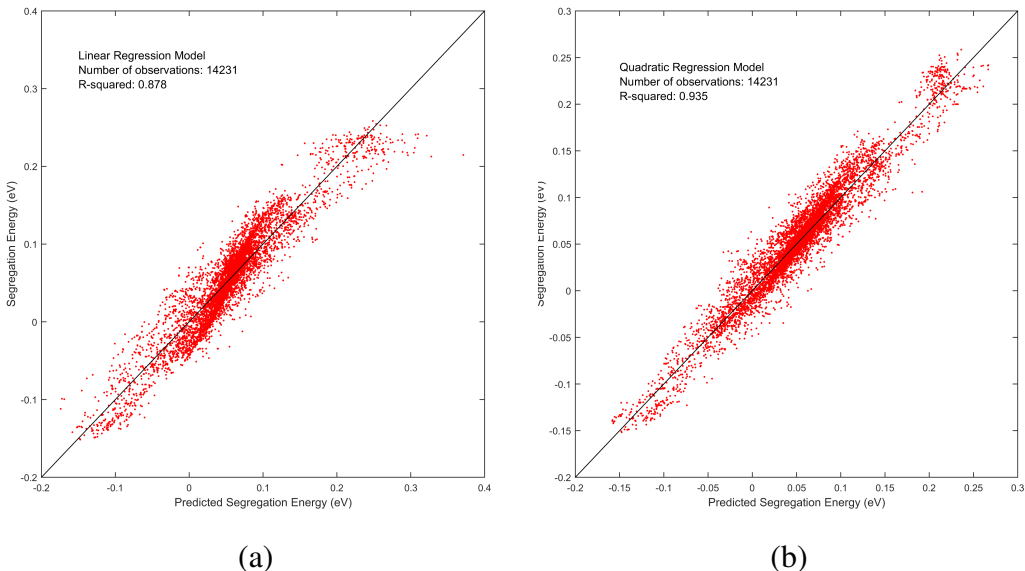


Fig. 11 Plots of model predictions against the atomistically calculated segregation energy for two different regression models based on the atomic metrics: (a) linear regression model and (b) quadratic regression model (with linear and interaction terms)

Figure 12 shows how neural network–predicted segregation energies compare to the atomistically calculated segregation energies. The neural network only uses one layer with 70% of the dataset used for the training set, 15% used for the validation

set, and 15% used for the test set. The model predicts the segregation energy quite well ($R^2 > 0.97$), and the residual error of the neural network model is Gaussian distributed about a mean of zero.

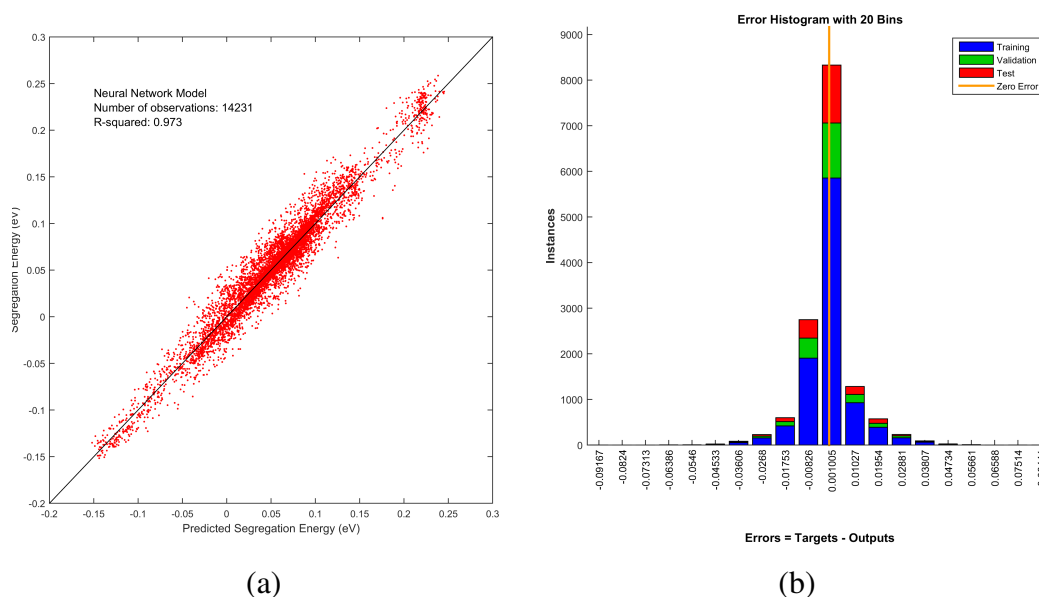


Fig. 12 (a) Plot of neural network model predictions against the atomistically calculated segregation energy, and (b) error histogram of the neural network model for the training set (70% of data), validation set (15%), and test set (15%)

The model can now be used to predict segregation energies in magnesium GBs. Figure 13 shows the predicted segregation energies from the neural network model as a function of spatial location within the boundary for the same GBs as shown in Fig. 8. Qualitatively, very similar trends in segregation energy with respect to spatial position exist for the atomistically calculated and neural network–predicted segregation energies. For a quantitative comparison of the two, Fig. 14 shows the prediction error as a function of spatial position. These images are for the same GBs, but the difference as a function of spatial position is shown both with the colorbar as well as the size of the atom position. The prediction error decreases as a function of distance from the center of the GB, and there are localized regions within the GB that have errors as large as 0.10 eV. However, errors of this magnitude occur only for a small percentage of atoms.

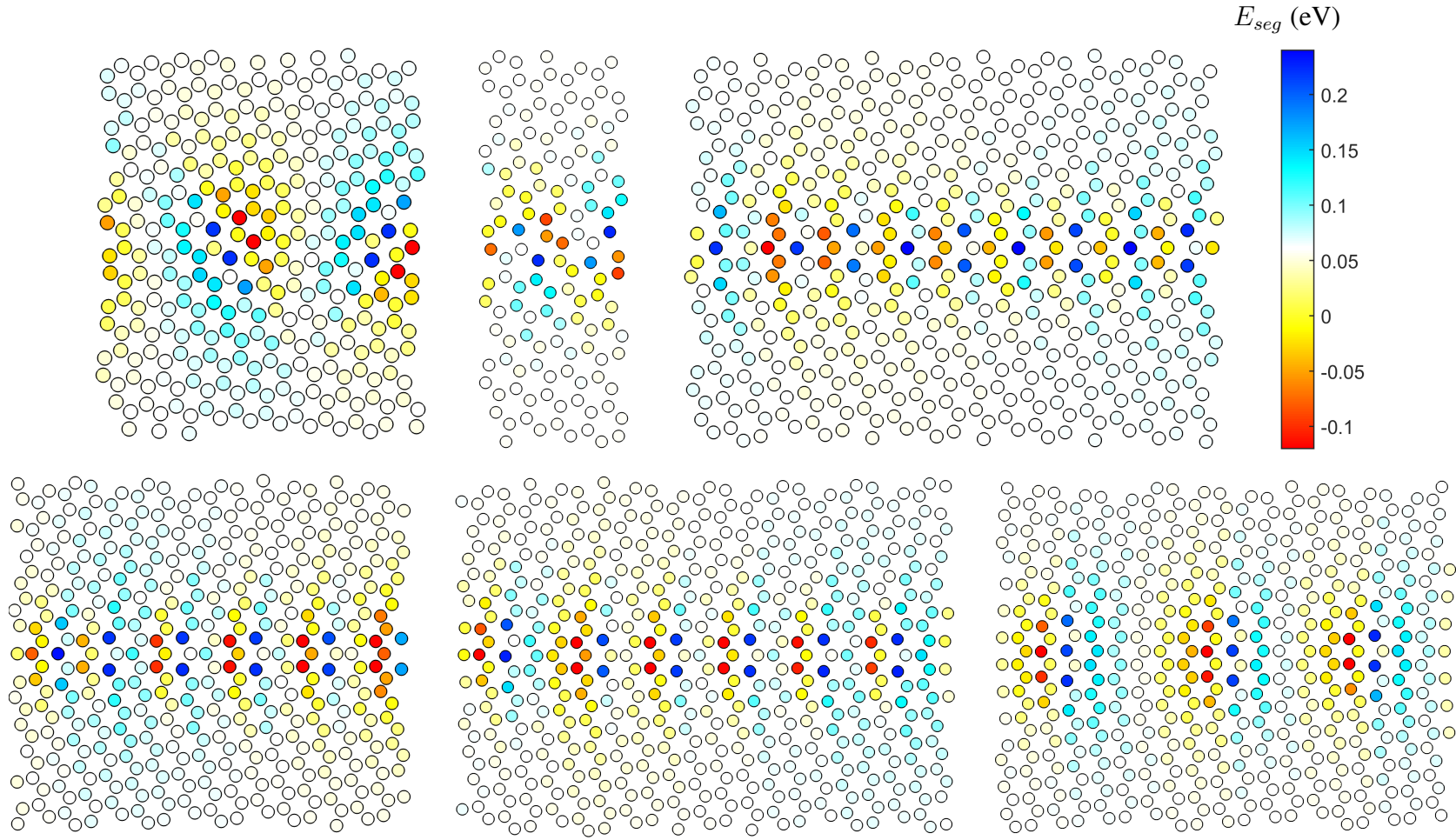


Fig. 13 Image of the neural network prediction of segregation energy E_{seg}^{NN} as a function of spatial location within the GB region for GBs with increasing GB misorientation angle within the $\langle 0001 \rangle$ STGB system: (top, left to right) $\{74\bar{3}0\}/\{3470\}$ GB, $\{32\bar{1}0\}/\{1230\}$ GB, $\{11, \bar{8}, \bar{3}, 0\}/\{3, \bar{8}, 11, 0\}$ GB, and (bottom, left to right) $\{97\bar{2}0\}/\{2790\}$ GB, $\{11, \bar{9}, \bar{2}, 0\}/\{2, \bar{9}, 11, 0\}$ GB, $\{10, \bar{9}, \bar{1}, 0\}/\{1, \bar{9}, 10, 0\}$ GB. Compare with actual energies in Fig. 8.

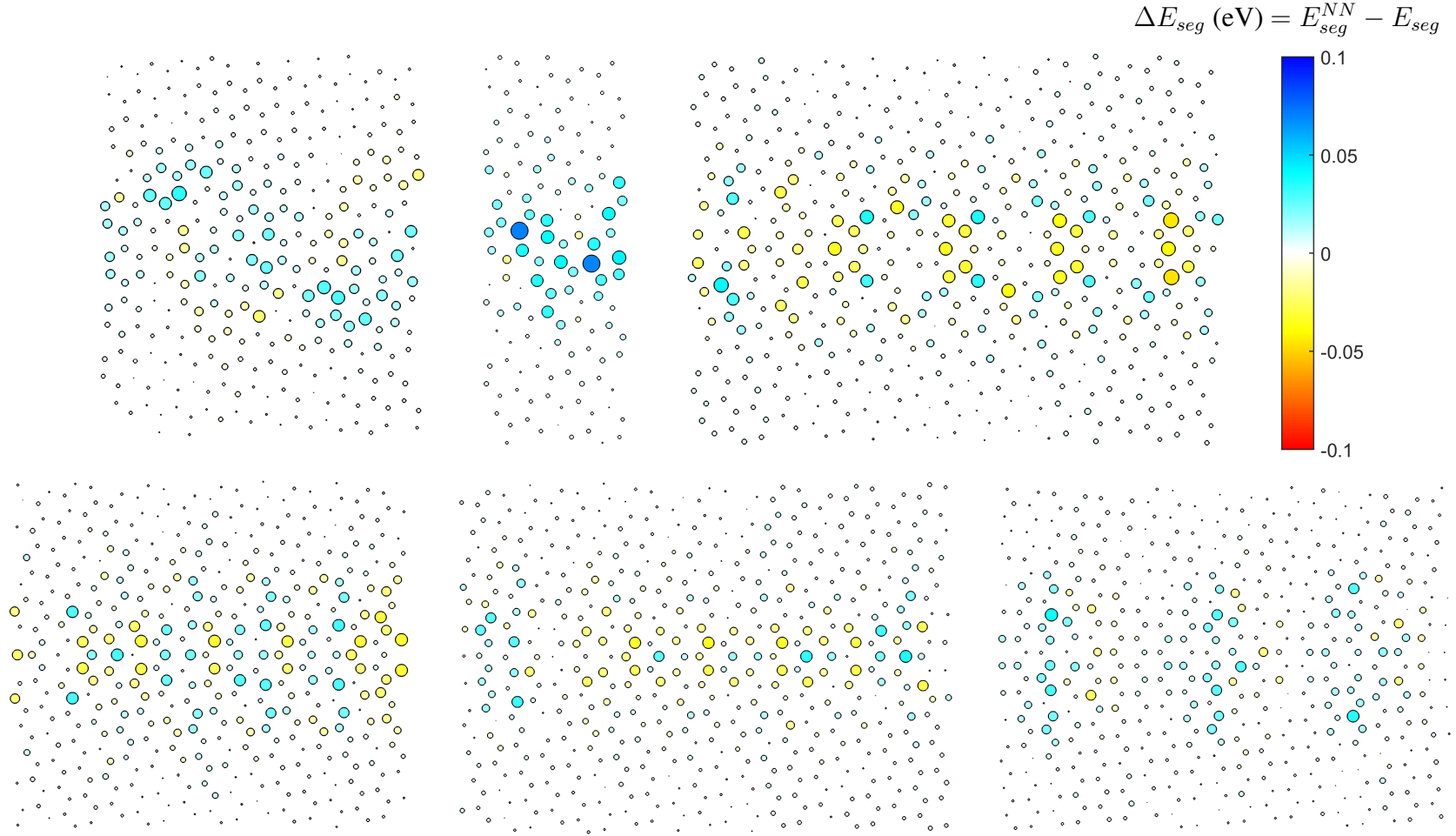


Fig. 14 Image of the neural network prediction error of segregation energy ΔE_{seg} as a function of spatial location within the GB region for GBs with increasing GB misorientation angle within the $\langle 0001 \rangle$ STGB system: (top, left to right) $\{74\bar{3}0\}/\{3\bar{4}70\}$ GB, $\{32\bar{1}0\}/\{1\bar{2}30\}$ GB, $\{11, \bar{8}, \bar{3}, 0\}/\{\bar{3}, \bar{8}, 11, 0\}$ GB, and (bottom, left to right) $\{97\bar{2}0\}/\{2790\}$ GB, $\{11, \bar{9}, \bar{2}, 0\}/\{\bar{2}, \bar{9}, 11, 0\}$ GB, $\{10, \bar{9}, \bar{1}, 0\}/\{\bar{1}, \bar{9}, 10, 0\}$ GB. To further accentuate the location and magnitude of error, the size of the atoms is scaled by increasing absolute value of error (scaled from minimal size to three times the size of those in Figs. 8 and 13 for every 0.10-eV error).

The following framework can be applied to understanding segregation of substitutional atoms to GBs. First and foremost, a predictive model for segregation can provide atomic segregation energies of large atomic configurations very rapidly without running additional simulations for each potential site. This model can be used to speed up potential swap states in kinetic Monte Carlo (atomistic) simulations or to give information about an average segregation energy (or segregation potential) for higher-scale models. As an example, the model used herein was applied to one of the larger GBs (19,624 atoms) within the $\langle 0001 \rangle$ STGB system—the $\{26, \bar{1}7, \bar{0}, 0\}/\{\bar{0}, \bar{1}7, 26, 0\}$ GB. Figure 15 shows the results. Interestingly, with the predictive model, the segregation energies have very little computational cost (on the order of fractions of a second) whereas using molecular statics to compute the segregation energies for each of the 19,624 atomic sites would have easily been at least 4–6 orders of magnitude higher. This computational cost will only be magnified for 1,000,000 atom simulations of nanocrystalline materials or in cases where these values need to be iteratively calculated (e.g., Monte Carlo simulations). While this study tackles the problem of predicting the segregation energy for a single atom using a neighborhood of only magnesium, it would also be informative to have a model that can account for substitutional atoms (e.g., aluminum in this study) in the local environment. Clearly, the ability to compute GB physical properties of interest using machine learning techniques can have broad implications for the area of GB science and engineering.

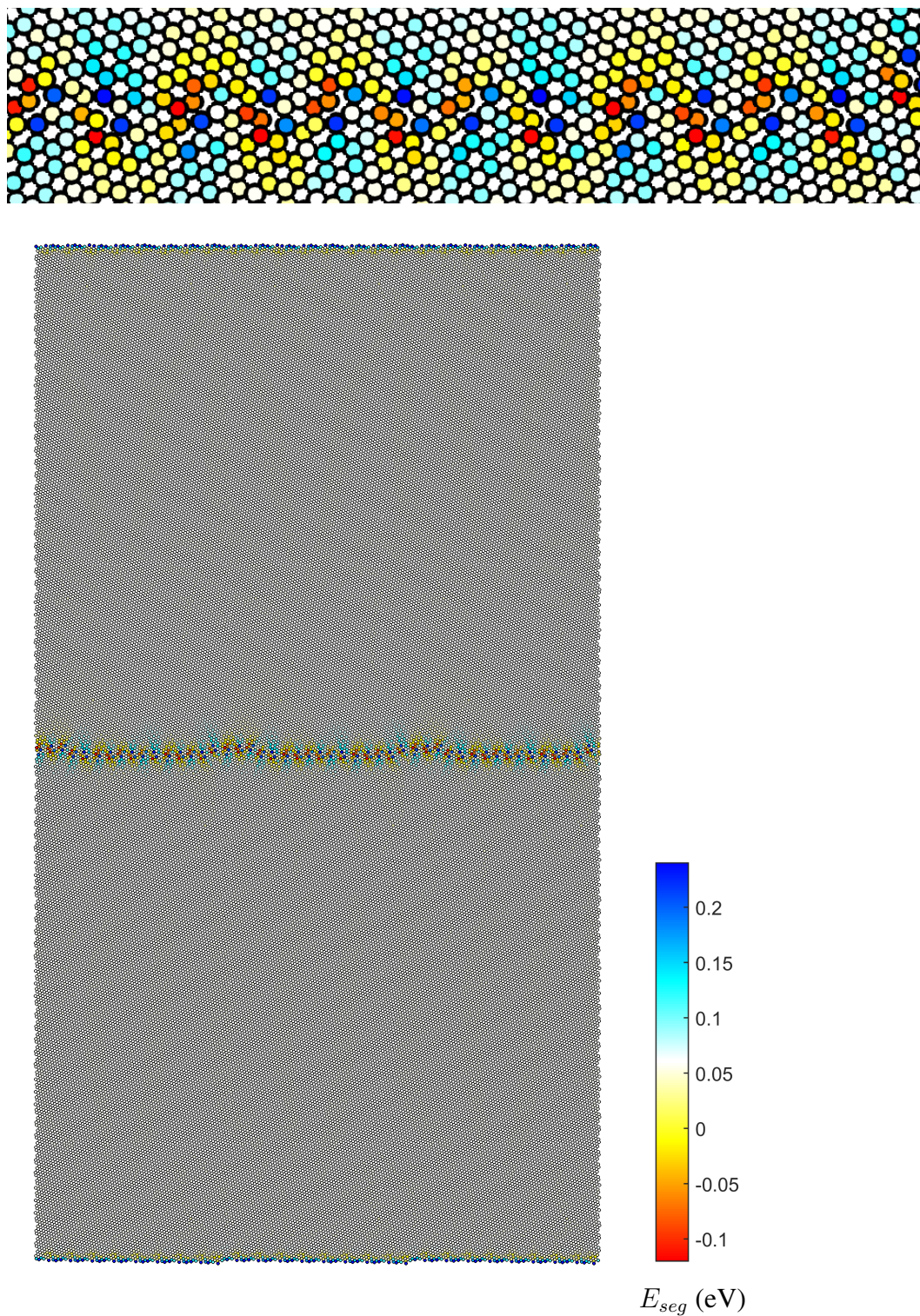


Fig. 15 Images of the neural network prediction of the segregation energy E_{seg}^{NN} as a function of spatial location for the 19,624 atoms in the $\{26, \bar{1}7, 9, 0\}/\{\bar{9}, \bar{1}7, 26, 0\}$ GB as viewed along the $\langle 0001 \rangle$ tilt direction. The bottom image is of the whole boundary, while the top image is a magnified view of part of the boundary.

4. Conclusion

Engineering magnesium alloys for Army applications requires an understanding of corrosion behavior, including how GBs or second phases/intermetallics affect corrosion at the atomic scale. In magnesium–aluminum alloys, precipitation of the $\text{Mg}_{17}\text{Al}_{12}$ phase at GBs can have important implications for mechanical and corrosion behavior. The objective of this study is to quantify the energetics of segregation of aluminum to a dataset of different STGBs for magnesium. In this work, aluminum atoms were iteratively placed at various atomic sites within 20 Å of the GB center for a dataset of 30 $\langle 0001 \rangle$ STGBs. Results show how GB structure affects the energetics and length scales of aluminum segregation as well as the dependence of segregation energetics on the local atomic environment, which was used to form a surrogate (machine learning) model for segregation energetics. The neural network model predicts segregation energies that are comparable to atomistically-calculated energies ($R^2 > 0.97$) and is obviously much more efficient than atomistically calculating the GB segregation energies. This model was then applied to one of the larger GB structures to show the ability to predict segregation energy over a large number of atoms while retaining the high-fidelity energetic calculations at the boundary. The ability to compute GB physical properties of interest using machine learning techniques can have broad implications for the area of GB science and engineering.

5. References

1. Esmaily M, Svensson JE, Fajardo S, Birbilis N, Virtanen S, Arrabal R, Thomas S, Johansson LG. Fundamentals and advances in magnesium alloy corrosion. *Prog Mater Sci.* 2017;89:92–193.
2. Barrett CD, Imandoust A, El Kadiri H. The effect of rare earth element segregation on grain boundary energy and mobility in magnesium and ensuing texture weakening. *Scr Mater.* 2018;146:46–50.
3. Barrett CD, Imandoust A, Oppedal AL, Inal K, Tschopp MA, El Kadiri H. Effect of grain boundaries on texture formation during dynamic recrystallization of magnesium alloys. *Acta Mater.* 2017;128:270–283.
4. Tschopp MA, McDowell DL. Asymmetric tilt grain boundary structure and energy in copper and aluminium. *Phil Mag.* 2007;87(25):3871–3892.
5. Tschopp MA, McDowell DL. Structural unit and faceting description of $\Sigma 3$ asymmetric tilt grain boundaries. *J Mater Sci.* 2007;42(18):7806–7811.
6. Tschopp MA, McDowell DL. Structures and energies of $\Sigma 3$ asymmetric tilt grain boundaries in copper and aluminium. *Phil Mag.* 2007;87(22):3147–3173.
7. Spearot DE, Tschopp MA, Jacob KI, McDowell DL. Tensile strength of $\langle 100 \rangle$ and $\langle 110 \rangle$ tilt bicrystal copper interfaces. *Acta Mater.* 2007;55(2):705–714.
8. Tschopp MA, McDowell DL. Dislocation nucleation in $\Sigma 3$ asymmetric tilt grain boundaries. *Int J Plast.* 2008;24(2):191–217.
9. Tschopp MA, Tucker GJ, McDowell DL. Atomistic simulations of tension-compression asymmetry in dislocation nucleation for copper grain boundaries. *Comput Mater Sci.* 2008;44(2):351–362.
10. Adlakha I, Bhatia MA, Tschopp MA, Solanki KN. Atomic scale investigation of grain boundary structure role on intergranular deformation in aluminium. *Phil Mag.* 2014;94(30):3445–3466.
11. Adlakha I, Tschopp MA, Solanki KN. The role of grain boundary structure and crystal orientation on crack growth asymmetry in aluminum. *Mater Sci Eng.* 2014;A618:345–354.

12. Tschopp MA, Horstemeyer MF, Gao F, Sun X, Khaleel M. Energetic driving force for preferential binding of self-interstitial atoms to Fe grain boundaries over vacancies. *Scr Mater.* 2011;64(9):908–911.
13. Tschopp MA, Solanki KN, Gao F, Sun X, Khaleel MA, Horstemeyer MF. Probing grain boundary sink strength at the nanoscale: energetics and length scales of vacancy and interstitial absorption by grain boundaries in α -Fe. *Phys Rev B.* 2012;85(6):064108.
14. Rajagopalan M, Tschopp MA, Solanki KN. Grain boundary segregation of interstitial and substitutional impurity atoms in alpha-iron. *JOM.* 2014;66(1):129–138.
15. Rhodes NR, Tschopp MA, Solanki KN. Quantifying the energetics and length scales of carbon segregation to α -Fe symmetric tilt grain boundaries using atomistic simulations. *Modell Simul Mater Sci Eng.* 2013;21(3):035009.
16. Solanki KN, Tschopp MA, Bhatia MA, Rhodes NR. Atomistic investigation of the role of grain boundary structure on hydrogen segregation and embrittlement in α -Fe. *Metall Trans A.* 2013;44A:1365–1375.
17. Tschopp MA, Gao F, Yang L, Solanki KN. Binding energetics of substitutional and interstitial helium and di-helium defects with grain boundary structure in α -Fe. *J Appl Phys.* 2014;115:033503.
18. Tschopp MA, Gao F, Solanki KN. Binding of He_nV clusters to α -Fe grain boundaries. *J Appl Phys.* 2014;115(23):233501.
19. Tschopp MA, Gao F, Solanki KN. He–V cluster nucleation and growth in α -Fe grain boundaries. *Acta Mater.* 2017;124:544–555.
20. Van Beers PRM, Kouznetsova VG, Geers MGD, Tschopp MA, McDowell DL. A multiscale model of grain boundary structure and energy: From atomistics to a continuum description. *Acta Mater.* 2015; 82:513–529.
21. Tschopp MA, Coleman SP, McDowell DL. Symmetric and asymmetric tilt grain boundary structure and energy in Cu and Al (and transferability to other fcc metals). *IMMI.* 2015;4(1):11–21.
22. Liu XY, Ohotnicky PP, Adams JB, Rohrer CL, Hyland RW. Anisotropic surface segregation in Al-Mg alloys. *Surf Sci.* 1997;373:357–370.

23. NIST Interatomic Potentials Repository:[accessed 2018 Sep 5].
<https://www.ctcms.nist.gov/potentials/entry/1997-Liu-X-Y-Ohotnicky-P-P-Adams-J-B-et-al-Al-Mg/>

List of Symbols, Abbreviations, and Acronyms

1nn	first nearest neighbor
3-D	three-dimensional
Al	aluminum
EAM	embedded atom method
fcc	face centered cubic
GB	grain boundary
hcp	hexagonal close packed
LAMMPS	Large-scale Atomic/Molecular Massively Parallel Simulator
MD	molecular dynamics
Mg	magnesium
NIST	National Institute of Standards and Technology
STGB	symmetric tilt grain boundaries

1 DEFENSE TECHNICAL
(PDF) INFORMATION CTR
DTIC OCA

2 DIR ARL
(PDF) IMAL HRA
RECORDS MGMT
RDRL DCL
TECH LIB

1 GOVT PRINTG OFC
(PDF) A MALHOTRA

1 RDRL D
(PDF) M TSCHOPP